THE JOURNAL OF PHYSICAL CHEMISTRY C

pubs.acs.org/JPCC

Article

$TiNb_2O_7$ and VNb_9O_{25} of ReO_3 Type in Hybrid Mg−Li Batteries: Electrochemical and Interfacial Insights

Sebastian Maletti,* Abraham Herzog-Arbeitman, Steffen Oswald, Anatoliy Senyshyn, Lars Giebeler, and Daria Mikhailova*

Cite This: J. Phys. Chem. C 2020, 124, 25239−25248

Read Online

ACCESS | Metrics & More | Article Recommendations | Supporting Information

ABSTRACT: As one of the beyond-lithium battery concepts, hybrid metal-ion batteries have aroused growing interest. Here, $TiNb_2O_7$ (TNO) and VNb_9O_{25} (VNO) materials were prepared using a high-temperature solid-state synthesis and, for the first time, comprehensively examined in hybrid Mg−Li batteries. Both materials adopt ReO_3-related structures differing in the interconnection of oxygen polyhedra and the resulting guest ion diffusion paths. We show applicability of the compounds in hybrid cells providing capacities comparable to those reached in Li-ion batteries (LIBs) at room temperature (220 mAh g^{-1} for TNO and 150 mAh g^{-1} for VNO, both at 0.1 C), their operability in the temperature range between −10 and 60 °C, and even better capacity retention than in pure LIBs, rendering this hybrid technology superior for long-term application. Post mortem X-ray photoelectron spectroscopy reveals a cathode−electrolyte interface as a key ingredient for providing excellent electrochemical stability of the hybrid battery. A significant contribution of the intercalation pseudocapacitance to charge storage was observed for both materials in Li- and Mg−Li batteries. However, the pseudocapacitive part is higher for TNO than for VNO, which correlates with structural distinctions, providing better accessibility of diffusion pathways for guest cations in TNO and, as a consequence, a higher ionic transport within the crystal structure.

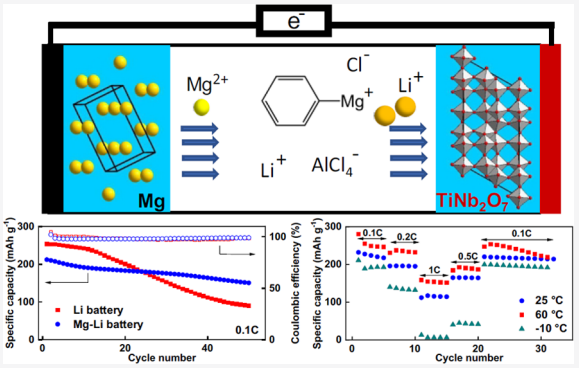

1. INTRODUCTION

As lithium-ion batteries have become one of the most widespread energy storage technologies in recent decades, the shortage of needed resources represents a potential future scenario. To circumvent this issue, changes to the composition of conventional electrode materials appear as the quickest and easiest solution at first glance. A further important approach is found in the possibility of replacing the typical lithium-ion battery chemistry itself. Nonaqueous magnesium-ion batteries have attracted substantial interest since they were successfully introduced by Aurbach's group in 2000.[1] However, their applicability is still very ambitious, as positive electrode materials which can reliably insert divalent cations are only rarely known.[2] A very promising approach to overcome this issue is the concept of hybrid Mg−Li batteries, which contain a dual-salt electrolyte that provides both Mg- and Li-ions and therefore allows the use of known lithium intercalation compounds together with Mg anodes. This concept had been proposed for the first time in 2014 using a $LiFePO_4$ cathode, which inserts Li only, while Mg carries out the anodic reaction, as concluded from post mortem X-ray diffraction (XRD) investigations.[3] However, stable operation over only seven cycles was demonstrated in that work, and significant optimization was required for broad applicability. Since then, Mg−Li batteries have been studied by many researchers.[4] Firstly, considerable efforts were made using Chevrel phase Mo_6S_8 as a cathode, showing two reaction plateaus at 1.7 and 1.3 V during Mg insertion.[5] Using this material, long-term operation of 3000 cycles was realized, and the insertion mechanism was clarified as a concentration-dependent co-insertion of Li and Mg.[5,6] Similarly, studies on $MgCo_2O_4$ revealed intercalation of both cations in the cathodic redox process.[7] With the application of different TiO_2 polymorphs, it was understood that the structure and morphology strongly influence the electrochemical behavior in hybrid cells.[8] For conversion systems, the concept of a hybrid Mg−Li battery seems to be applicable as well. For example, in FeS_x conversion cathodes, the exclusive cathodic participation of Li was proposed.[9] As of now, many hybrid Mg−Li batteries have been reported with partially outstanding properties,[10] but a systematic comparison of underlying electrochemical processes

Received: August 12, 2020
Revised: September 22, 2020
Published: November 5, 2020

and mechanisms in Li- and hybrid Mg−Li batteries is still not performed.

One of the important issues concerning Mg−Li batteries is their electrolyte. Still, there is no standard electrolyte system for hybrid Mg−Li batteries. It was known that Mg can be reversibly deposited from ethereal solutions containing Grignard reagents RMgX with R = alkyl or aryl and X = Cl or Br, which however, show weak anodic stability (<1 V).[11] A further electrolyte design toward an enhanced stability window led to a so-called "all-phenyl-complex" (APC) electrolyte family, representing tetrahydrofuran (THF) solutions of $PhMgCl_2$−$AlCl_3$ with different species proportions, which exhibit highly reversible Mg deposition with almost 100% cycling efficiency, low overpotentials of less than 0.2 V, and an electrochemical window of about 3 V.[12] For hybrid Mg−Li batteries, LiCl in different concentrations is usually added as a Li source.[4] However, these electrolytes are not suitable for cathode materials having intermediate cell potentials since noninert current collectors and steel battery housings become unstable above 2.2 V.[13,14]

Therefore, for operation in conventional cell designs, electrode materials having a reaction potential below 2 V vs Mg^{2+}/Mg would be preferable. Of course, this significantly reduces the potential energy density of the battery. However, other parameters like cost and enhanced long-term cycling life of a Mg−Li battery can compensate for the loss in energy density.

At the moment, not much is known about the applicable temperature range of hybrid Mg−Li batteries. Although the APC electrolyte without any Li-salt has been found to be stable up to 180 °C[15] and a positive effect of high temperatures on the performance of Mg batteries with APC electrolytes has been reported,[16] only the low-temperature range was investigated for hybrid Mg−Li batteries with an APC electrolyte and Li-salt so far.[17]

Recently, a group of oxidic compounds, known as Wadsley−Roth phases, have gained a lot of attention as electrode materials for Li-ion batteries because of their exceptionally large capacities at high current densities. They crystallize in ReO_3-like structures with shear planes, leading to blocks of corner-sharing octahedra, which are connected to each other via edges. A facilitated Li-diffusion within the crystal structure is supposed to be the reason for the high rate capability. The best-known examples are Nb_2O_5[18] and $Ti_2Nb_{2x}O_{4+5x}$ materials,[19] which show a large pseudocapacitive contribution to the entire specific capacity in Li batteries. However, there is no information about electrochemical behavior of such materials in hybrid Mg−Li batteries.

Hence, we investigated $TiNb_2O_7$ (TNO) and VNb_9O_{25} (VNO), both adopting ReO_3-like structures, as electrode materials and model systems to evaluate the influences of slight structural differences on their electrochemical behavior in Mg−Li hybrid batteries. TNO is currently under extensive investigation in lithium-ion batteries since it was proposed by J. B. Goodenough as the successor of the well-known $Li_4Ti_5O_{12}$ in 2011.[20] Its large capacity and favorable smooth potential curve render it a very promising material for the next generation of batteries. VNO has been studied much less, but recent reports show encouraging electrochemical performance in Li batteries.[21−23] The crystal structure of both materials consists of edge- and corner-sharing ReO_3-type octahedra, where the VNO structure is distinct from the TNO structure as the vanadium cation is tetrahedrally oxygen coordinated.

Herein, we report an in-depth investigation of the electrochemical behavior of $TiNb_2O_7$ and VNb_9O_{25} with the aims to (i) test their applicability in hybrid Mg−Li batteries in a broad temperature range, (ii) compare kinetic characteristics of both materials in Li- and hybrid Mg−Li batteries, (iii) provide the proof of correlation with the structural issues of the cathodes, and (iv) evaluate the ability of electrodes for a long-term cycling under moderate current rates.

2. EXPERIMENTAL

2.1. Synthesis and Characterization. Micro-sized $TiNb_2O_7$ and VNb_9O_{25} were prepared by solid-state reactions using stoichiometric amounts of TiO_2 (Chempur, 99.9%), Nb_2O_5 (Alfa Aesar, 99.9985%), and NH_4VO_3 (Alfa Aesar, 99%). Pellets made from the reactants were placed in alumina crucibles and heated up to 1350 °C for 40 h in air, followed by slow cooling.

For a sol−gel synthesis of nano-sized $TiNb_2O_7$, stoichiometric amounts of titanium(IV) isopropoxide (Acros Organics, >98%), which was dried over molecular sieves for three days, and niobium pentachloride (Alfa Aesar, >99.9%) were stirred in water-free isopropanol at room temperature. After evaporation of the solvent, the resulting gel was dried at 80 °C and calcined for two hours at 800 °C.

For phase analysis, powder X-ray diffraction (XRD) was carried out using a STOE STADI P diffractometer equipped with a position-sensitive linear wire detector with Co $K_{\alpha 1}$ radiation (λ = 1.78896 Å) in transmission mode. Scanning electron microscopy (SEM) was applied to characterize particle morphologies. Therefore, a ZEISS Leo Gemini 1530 microscope was used with an in-lens detector at an acceleration voltage of 15 kV. EDX spectra were obtained using a Bruker EDXS spectrometer.

2.2. Neutron Powder Diffraction Studies. Elastic coherent neutron powder scattering was performed on the high-resolution powder diffractometer SPODI at the research reactor FRM-II (Garching, Germany) with monochromatic neutrons at λ = 1.5481(1) Å wavelength. Measurements were performed in Debye−Scherrer geometry.[24] The powdered samples (ca. 2 cm^3) were filled into a vanadium container of 10 mm diameter. Diffraction data were collected in air at 25 °C and then corrected for geometrical aberrations and the curvature of the Debye−Scherrer rings. For both diffraction studies, structural parameters were determined by Rietveld analyses based on all available reflections using the Fullprof program implemented in WinPLOTR software.[25]

2.3. Electrochemical Investigations. Electrochemical tests were performed in two-electrode Swagelok-type cells using a VMP3 potentiostat (Biologic Instruments) in a temperature window between −10 and 60 °C. Electrodes were prepared by compacting a mixture of the active material with Super P 65 carbon (BASF) and PTFE (Aldrich) in an 80:10:10 weight ratio onto a stainless steel or copper current collector. Magnesium and lithium chips (99.9%, G-Materials) were carefully mechanically polished and used as anodes. A glass fiber cloth (Whatman, GF/D), soaked with the electrolyte, served as a separator. All-phenyl-complex (APC) electrolytes were prepared by the reaction of stoichiometric amounts of $AlCl_3$ (99.985%, Alfa Aesar) and phenylmagnesium chloride (Sigma Aldrich) in THF (≥99.9%, Sigma Aldrich). For a comparison of different lithium sources, $LiBH_4$ (≥95.0%,

https://dx.doi.org/10.1021/acs.jpcc.0c07373
J. Phys. Chem. C 2020, 124, 25239−25248

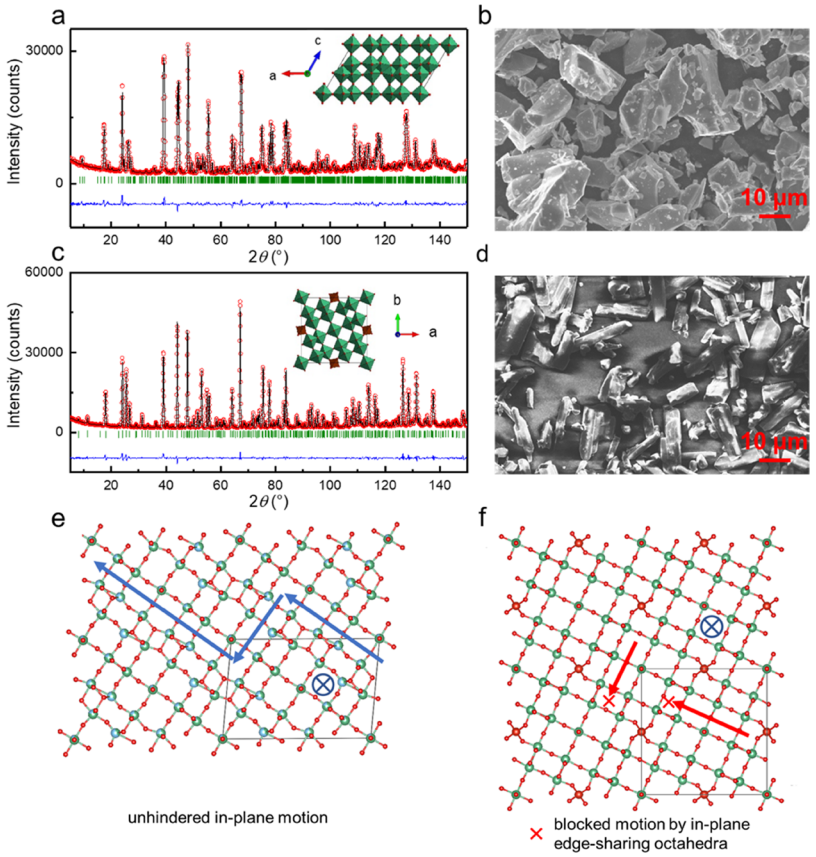

Figure 1. Neutron diffraction patterns of (a) $TiNb_2O_7$ and (c) VNb_9O_{25} with the difference curve (blue) between the experimental data (red) and calculated (black) curves. The corresponding crystal structures are shown in the insets. In $TiNb_2O_7$, Ti and Nb randomly occupy corner- and edge-sharing oxygen octahedra, whereas in VNb_9O_{25}, VO_4-tetrahedra are connected with NbO_6-octahedra via corners, and NbO_6-octahedra are corner- and edge-sharing with each other. SEM micrographs of (b) $TiNb_2O_7$ and (d) VNb_9O_{25}. Possible guest ion diffusion paths are indicated for (e) $TiNb_2O_7$ and (f) VNb_9O_{25} with blue arrows representing unhindered paths and red arrows representing blocked paths. The cross-in-circle symbol indicates directions perpendicular to the drawing plane, which are available for undisturbed diffusion. Ti, Nb, and V atoms are depicted as blue, green, and red spheres, respectively. Oxygen atoms are drawn as small red spheres.

Sigma Aldrich) and LiCl (99.9%, Alfa Aesar) were added to these solutions. The standard electrolyte was composed of 0.4 M $(PhMgCl)_2$-$AlCl_3$ + 1.5 M $LiBH_4$. Since a comparison confirmed similar, slightly improved electrochemical behavior when 1.25 M LiCl (see Figure S1) was used, this salt was used for further electrolyte preparation. Galvanostatic cycling with potential limitation (GCPL) was carried out in various potential windows, usually 0.3−1.4 V vs Mg^{2+}/Mg for TNO and 0.12−1.4 V vs Mg^{2+}/Mg for VNO, using multiple C-rates, where 1 C denotes the current necessary to insert 1 Li^+ or 0.5 Mg^{2+} per formula unit within one hour. Cyclic voltammetry (CV) was performed within the same potential windows as that applied for GCPL at scan rates ranging from 5 to 100 μV/s.

For galvanostatic intermittent titration (GITT) experiments, three-electrode Swagelok-type cells with metallic magnesium were used as both counter and reference electrodes. A current of 0.05 C was applied for 10 min. Before the next titration step, a rest period of 12 h followed to allow the determination of an open-circuit voltage (OCV) value near-equilibrium conditions. Chemical diffusion coefficients were calculated according to

$$\tilde{D} = \frac{4}{\pi}\left(\frac{m \cdot V_m}{M \cdot A}\right)^2 \cdot \left[\frac{\Delta E_s}{\tau \cdot \frac{dE}{d\sqrt{t}}}\right]^2$$

where m denotes the mass of the active material, M is its molar mass, V_m is the molar volume, and A is the electrode surface area. ΔE_s corresponds to the difference in OCV between two titration steps and τ denotes the duration of the applied current pulses.[22] The term $\frac{dE}{d\sqrt{t}}$ was calculated by derivation of the first half of a titration step. An example of a GITT titration step is provided in Figure S2.

2.4. X-ray Photoelectron Spectroscopy. For X-ray photoelectron spectroscopy studies, a PHI 5600 CI system with an Al Kα monochromatized X-ray source at 350 W and a hemispherical analyzer at a pass energy of 29 eV were used. The system base pressure was about 10^{-9} mbar. Low energy electrons were used to minimize surface charging. The binding energy scale was corrected with respect to the C 1s peak position of adventitious carbon at 284.8 eV. A quantification of elemental concentrations was performed using standard single element sensitivity factors.[26] Depth profiling was carried out by sputtering with Ar^+ ions at 3.5 keV, yielding an approximate erosion rate of 3 nm/min, as calibrated for a SiO_2 reference.

3. RESULTS AND DISCUSSION

3.1. Solid-State Synthesis. After calcination at 1350 °C, the ground TNO powder shows a yellowish color, while VNO appears light brown. To reliably distinguish the positions of different transition metals and their occupancy within the

https://dx.doi.org/10.1021/acs.jpcc.0c07373
J. Phys. Chem. C 2020, 124, 25239−25248

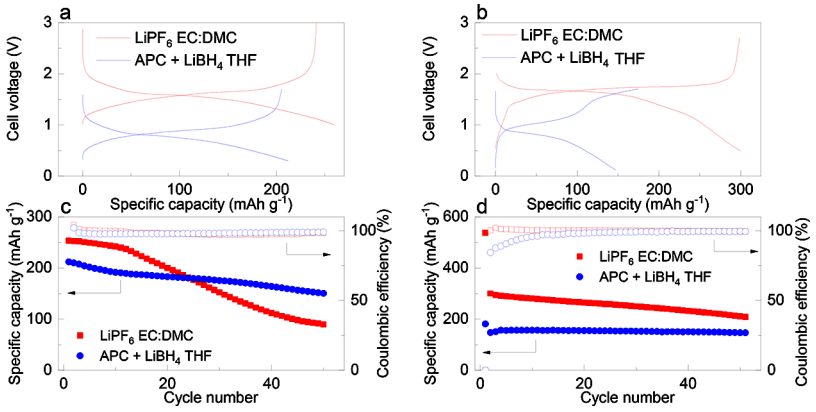

Figure 2. Charge−discharge curves of (a) $TiNb_2O_7$ and (b) VNb_9O_{25} in Li- and hybrid Mg−Li batteries, and discharge capacities with corresponding Coulombic efficiencies for (c) $TiNb_2O_7$ and (d) VNb_9O_{25}. All curves were obtained using a 0.1 C current at 25 °C.

crystallographic framework, neutron powder diffraction was applied. Figure 1 shows the NPD patterns of both compounds and the corresponding Rietveld analysis. Both compounds were obtained as phase-pure samples, also proven by XRD. The structure of TNO can be indexed to the monoclinic $C2/m$ setting (ICSD 48109), while VNO crystallizes in a tetragonal lattice in the space group $I\bar{4}$ (ICSD 73802).[27,28] Detailed structural information for both compounds is presented in the Supporting Information, Table S1.

As apparent from the SEM micrographs (Figure 1b,d), the high-temperature synthesis results in large particles in the range of 10−30 μm with irregular shapes for TNO and a preferred rod-like morphology for VNO. Similar to the related T-Nb_2O_5, well-known for its open network of Li diffusion pathways,[29] TNO and VNO provide a comparable host structure with some distinctions. Obviously, TNO allows cation diffusion along the *b*-axis and VNO along the *c*-axis (Figure 1e,f). Additionally, the migration in the *h*0*l* planes of TNO is favored, in contrast to VNO, where those paths are blocked by edge-sharing NbO_6 octahedra.

3.2. Electrochemical Characterization. Galvanostatic discharge−charge profiles of both micro-sized materials are shown in Figure 2. Note that these curves represent the situation after a formation cycle, as in the case of VNO an irreversible capacity loss occurs in the initial discharge, see Figure S3, which is usually attributed to an irreversible redox of V^{5+} to V^{3+} and the associated change to octahedral V−O coordination.[23] Obviously, TNO (Figure 2a) as well as VNO (Figure 2b) exhibit a lower voltage in hybrid Mg−Li batteries compared to a conventional Li-ion setup due to the difference of Mg^{2+}/Mg and Li^+/Li redox couples of approximately 0.7 V. However, the specific capacity of VNO is significantly lower in the case of the hybrid cell, TNO delivers almost the same capacity as in pure Li cells.

Figure 2c,d shows the cycling behavior of micro-sized TNO and VNO, respectively. Interestingly, hybrid Mg−Li cells reveal better capacity retention than Li-ion batteries, already at very low current densities and thus, nonstressful conditions for the anodic side. In the case of TNO, higher capacities for the hybrid battery were observed already after 25 cycles, compared to the pure Li battery. Several issues can contribute to the observed phenomena, such as different long-term electrolyte stabilities, different storage mechanisms, or most probably, different properties of the formed cathode−electrolyte interface (CEI). To compare the diffusion phenomena in TNO and VNO in both battery types, chemical Li-diffusion coefficients in TNO and VNO electrodes were measured at room temperature using the GITT technique (Figure 3). For the

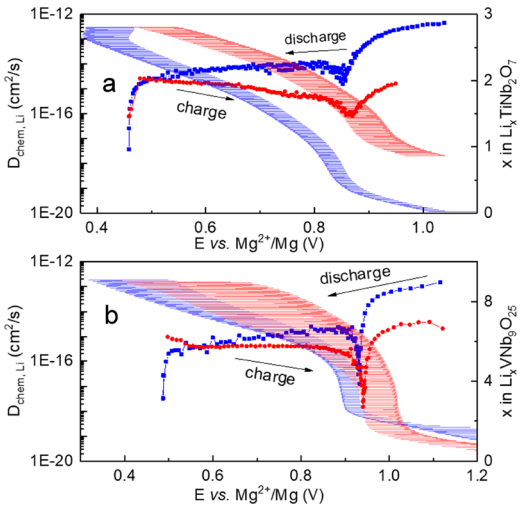

Figure 3. Chemical diffusion coefficients in (a) $TiNb_2O_7$ and (b) VNb_9O_{25} in hybrid Mg−Li batteries, determined from GITT measurements. The corresponding galvanostatic titration curve is indicated by shaded lines.

calculations, it was assumed that only Li cations were inserted into the solids since magnesium diffusion coefficients in oxides at room temperature are well below ~10^{-20} cm^2 s^{-1}.[30] Since micro-scale materials have been used, the semi-infinite diffusion model used in fundamental work[31] is applicable. Assuming a diffusion length of 1 μm and an average diffusion coefficient of 10^{-15} cm^2 s^{-1} yields $t = l^2/D$ of 10^8 s, which by far exceeds the duration of GITT pulses of 360 s and the corresponding relaxation times, thus fulfilling the criteria for semi-infinite diffusion.

In both compounds, diffusion coefficients range from ~5 × 10^{-12} to ~10^{-16} cm^2 s^{-1} and are dependent on the cell voltage, showing a sharp minimum, which matches well with the plateau observed in the discharge curves at roughly 0.85 V vs Mg^{2+}/Mg (TNO) and 0.92 V vs Mg^{2+}/Mg (VNO). Li diffusivity in TNO seems to be slightly higher than in VNO, varying between 5 × 10^{-12} cm^2 s^{-1} and ~10^{-15} in the potential window of 1.1−0.47 V vs Mg^{2+}/Mg. These values are in accordance with the presence of other crystallographic

https://dx.doi.org/10.1021/acs.jpcc.0c07373
J. Phys. Chem. C 2020, 124, 25239−25248

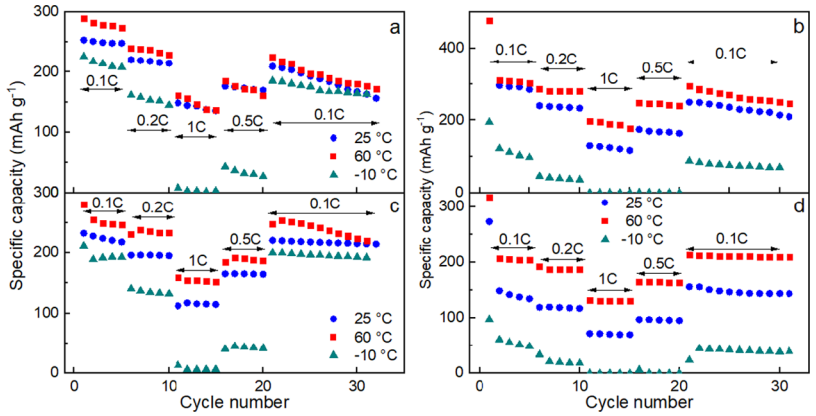

Figure 4. Rate capability tests of (a) $TiNb_2O_7$ and (b) VNb_9O_{25} at different temperatures in Li batteries (LP30) and (c, d) in hybrid Mg–Li batteries (0.4 M APC + 1.5 M $LiBH_4$).

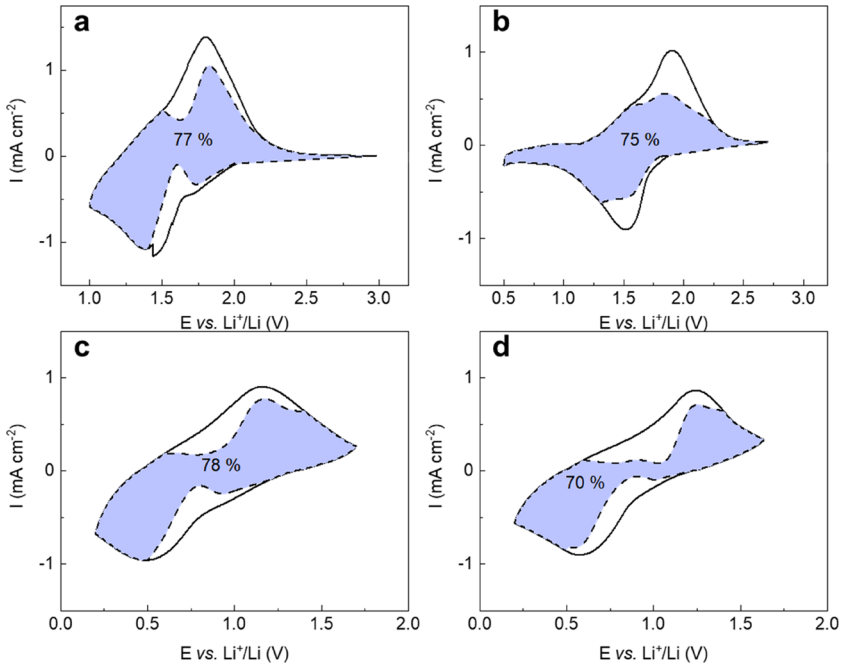

Figure 5. Cyclic voltammograms of (a) $TiNb_2O_7$ and (b) VNb_9O_{25} in Li batteries, and (c) $TiNb_2O_7$ and (d) VNb_9O_{25} in hybrid Mg–Li batteries at room temperature and a scan rate of 0.1 mV s^{-1}. The colored area represents the charge fraction that exhibits capacitive kinetics.

directions in TNO, offering additional charge carrier transport abilities, apart from the obvious cation diffusion path along the *b*-axis. However, VNO material barely supports diffusion pathways other than the one along the *c*-axis. A comparison with Li diffusion coefficients in Li batteries, shown in Figure S4, reveals that in average, hybrid Mg–Li batteries with both materials display a smoother trend and more stable behavior in the operated potential window. Note that D_{Li} available from the literature for the TNO material in Li cells provide similar values of $\sim 10^{-15}$–10^{-16} cm^2 s^{-1},[32] although they represent averaged values for the entire potential window, elaborated from electrochemical impedance spectroscopy (EIS) measurements on nano-structured materials. Similar values in the range of 10^{-15} cm^2 s^{-1} have been reported for VNO nanoribbons.[21]

The rate performance of both TNO and VNO compounds in Li- and hybrid Mg–Li batteries at temperatures of −10, 25, and 60 °C was studied, see Figure 4. It is evident that hybrid Mg–Li batteries with both TNO and VNO materials show a more stable cycling behavior than Li batteries at all temperatures. Generally, in both battery types, capacities of TNO and VNO significantly depended on the cycling rate, owing to a nonoptimized composite morphology. However, both materials in hybrid Mg–Li batteries demonstrate better capacity retention compared to Li batteries (Figure 4c,d). Although VNO yields much lower capacities in the case of the hybrid Mg–Li battery, and a more severe temperature dependence as compared to the Li battery (Figure 4d), it provides higher capacity retention and higher reversibility in the dual-salt setup. When cycled at 0.1 C again after the rate capability test, both materials return to their initial trend for Mg–Li batteries, which is not observed for the Li cells. Compared to the recently published application of $Li_3V_2(PO_4)_3$ in hybrid Mg–Li batteries, which deliver approximately 130 mAh g^{-1} at a current density of 1 C, our materials exhibit slightly lower capacities, which is mainly attributed to the nonoptimized electrode fabrication. More importantly, our results demonstrate the successful operation at 60 °C with even enhanced performance. A comparison

https://dx.doi.org/10.1021/acs.jpcc.0c07373
J. Phys. Chem. C 2020, 124, 25239–25248

between TNO and VNO leads us to the main conclusion that TNO behaves in a less temperature-dependent manner in both battery types, indicating a less diffusion-controlled mechanism.

As already mentioned in the Introduction section, Wadsley–Roth phases are known for their relatively weak dependence of the specific capacity on the current density, compared to other classes of electrode materials. The reason for this is a significant pseudocapacitive contribution to the total capacity. To distinguish between capacitive and diffusion-limited processes, we carried out sweep-dependent cyclic voltammetry measurements. At an increasing sweep rate, the intensity of the current response as well as the peak positions might change, allowing a quantitative determination of contributions to the storage mechanism. The current response in cyclic voltammetry represents a superposition of double-layer charging, pseudocapacitive currents, and diffusion-limited currents. Generally, the measured current i follows a power-law relation with the sweep rate v:[31]

$$i = av^b \tag{1}$$

An expontential coefficient of $b = 0.5$ represents a completely diffusion-controlled process, while for an exclusively capacitive reaction, $b = 1$. In our case, b adopts values between 0.6 and 0.7 (see Figure S5a for an example), indicating the presence of both diffusion-limited and capacitive currents.

As capacitive currents (k_1) relate linearly with v and diffusion-controlled currents (k_2) exhibit a square root relation with v, eq 1 can be expanded to[33]

$$i = k_1 v + k_2 v^{1/2} \tag{2}$$

By measuring CVs at various sweep rates, a linear fit of $i/v^{1/2}$ vs $v^{1/2}$ can be performed according to

$$i/v^{1/2} = k_1 v^{1/2} + k_2 \tag{3}$$

This allows obtaining k_1 as the slope and k_2 as the y-axis intercept.

An example of such a linear regression is given in Figure S5b. By performing these calculations, a separation of diffusion-limited currents from capacitive currents is quite easy since the former exhibit a square root sweep rate dependence and the latter linear sweep rate dependence. A separation between charging of the electrochemical double-layer and pseudocapacitive currents is less trivial since both processes follow the same time constant. However, since the effect of pure double-layer capacitance is usually 1 or 2 orders of magnitude smaller than the one of pseudocapacitance, its influence is neglected in further discussion.[34] Figure 5 shows the CV measured at 100 μV s^{-1} with the capacitive storage contribution obtained by calculating k_1 and k_2 at different potentials, shown as a blue-colored area. In lithium batteries, TNO and VNO exhibit similar capacitive fractions, see Figure 5a,b. In hybrid Mg–Li batteries, a very close capacitive storage value is observed for TNO, thus confirming a similar charge storage mechanism in both battery types. For VNO, a slight decrease of the capacitive contribution might be interpreted as decelerated kinetics in Mg–Li batteries. However, we suppose it originates mainly from the different potential cutoff during measurements in both kinds of cells.

The capacitive behavior of $TiNb_2O_7$ in Li-ion batteries has already been discussed in a previous report.[35] Interestingly, the capacitive contribution of 77% to the total capacity for micro-sized TNO (present work) is significantly higher than that for nano-sized TNO materials. For example, a capacitive contribution of about 57.5% was detected for TNO nanoparticles of 60 nm,[35] or 53%,[36] both studied at the same scan rate of 0.1 mV s^{-1}.

Note, the capacitive contribution does not necessarily imply an adsorption-based reaction as it is present in typical supercapacitor electrodes. Instead, the term "intercalation pseudocapacitance" has been defined by Augustyn et al.,[37] referring to an intercalation mechanism which, however, follows a capacitive time constant. They attributed this behavior, first observed in T-Nb_2O_5, to its open structure, which allows rapid bulk diffusion on a timescale that is usually observed for capacitor materials only. $TiNb_2O_7$ exhibits mostly a tunnel-like structure with an unhindered pathway for cations along one direction and partially limited pathways for other directions, thus providing less accessibility for guest cations than T-Nb_2O_5 and, consequently, a less capacitive behavior. Compared to VNb_9O_{25}, however, the Ti-containing compound shows almost one and a half as large capacitive contribution, which we also attribute to differences in the crystal structures. While the TNO structure consists mainly of corner-shared oxygen polyhedra and offers possible diffusion channels in several directions, the VNO structure contains more rigid edge-shared oxygen octahedra and is strictly limited to 1D diffusion.

As already mentioned, especially for TNO, there is almost no difference in the capacitive-like charge fraction in the two electrolyte systems used in Li- and Mg–Li batteries. The key to understanding this lies in the consideration of desolvation energies of Li and Mg cations and ionic conductivities of corresponding electrolytes. Desolvation energies for Mg cations in Cl^--containing THF solutions lie between 46 and 61 kJ/mol[38] and are even lower than desolvation energies for Li cations in carbonate-based electrolytes with $LiPF_6$ (~70 kJ/mol).[39] Room temperature ionic conductivities of the LP30 electrolyte (10 mS cm^{-1})[40] and APC composed of 0.8 M PhMgCl and 0.4 M $AlCl_3$ in THF (4 mS cm^{-1})[12] are comparable and can partially explain the observed similarities in the capacitive contribution. Although the influence of the Li salt ($LiBH_4$ or LiCl) present in the APC electrolyte on the conductivity is still unknown, the obtained results demonstrate that APC + LiCl electrolytes in hybrid Mg–Li batteries perform just as well as LP30 in Li batteries. In other words, our results prove that the hybrid battery concept allows to overcome poor kinetics of multivalent ion batteries by employing materials with a big capacitive contribution and to boost their performance to the range of LIBs.

3.3. Cathode–Electrolyte Interface (CEI) Studies. The comparison of electrolyte properties and charge storage mechanisms in TNO and VNO in Li- and hybrid Mg–Li batteries revealed large similarities, which are responsible for satisfactory performance of these materials in hybrid batteries. However, the reason for the better cycling behavior of hybrid batteries on the long-timescale is still not clear. To clarify the more stable cycling of $TiNb_2O_7$ and VNb_9O_{25} in Mg–Li batteries, the electrodes were investigated by post mortem X-ray photoelectron spectroscopy (XPS) analysis. Figure 6 presents XP spectra obtained at a TNO surface in the first discharged state and after 50 cycles, also in the discharged state, meaning a cutoff of Li batteries at 1 V and Mg–Li batteries at 0.3 V and their immediate disassembling. The spectra of VNO electrodes after the same testing procedure are given in Figure S7. First, Li battery CEI is discussed. The C 1s

https://dx.doi.org/10.1021/acs.jpcc.0c07373
J. Phys. Chem. C 2020, 124, 25239–25248

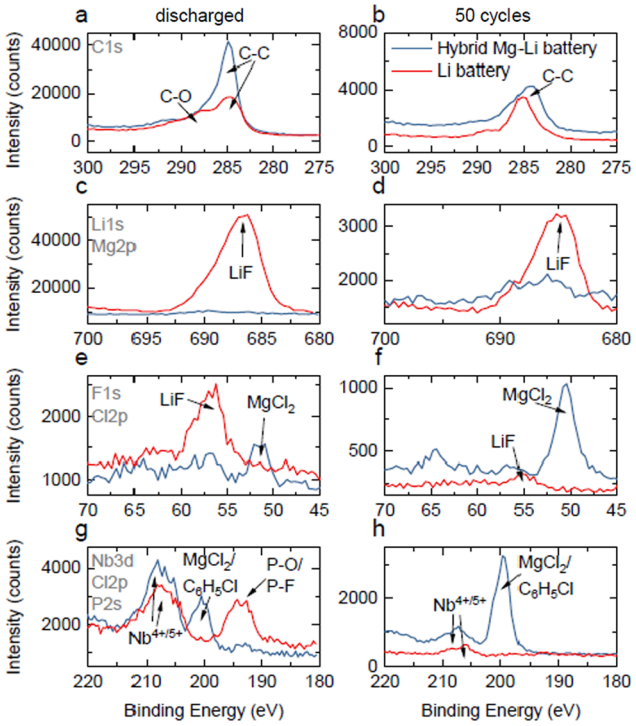

Figure 6. X-ray photoelectron spectra of the surface of a TNO electrode (a, c, e, g) after the first discharge down to 1 V in Li- and 0.3 V in Mg−Li cells, and (b, d, f, h) after 50 cycles in different binding energy ranges.

spectra (Figure 6a) reveal a significant contribution of organic and inorganic carbonates in the discharged state. This observation is in agreement with typical interface compositions in LIBs, as the presence of ethylene carbonate usually results in a formation of lithium ethylene dicarbonate (LEDC).[41] A large contribution in the F 1s spectrum (Figure 6c) is assigned to LiF formation,[26] which is also confirmed in the Li 1s binding energy (BE) region (Figure 6e).[42] The Nb 3d spectrum confirms the presence of Nb on the surface (Figure 6g), indicating that the interface has a limited thickness in this state, estimated to be less than 20 nm, which is penetrated by a Nb signal from the bulk material. The P 2s signal indicates the presence of phosphates,[43] as the decomposition of $LiPF_6$ usually results in P−O and P−F-containing species.[44] After 50 cycles, the contribution of carbonates, initially visible for the LIB, has decreased, and mainly C−C bonds remain (Figure 6b), although a slight shift to higher energies might be caused by the formation of C−OH bonds, suggesting that a growing organic layer buries the electrode surface. This hypothesis is confirmed by the diminishing signal of LiF (Figure 6d), which is much less intense than after the first discharge. Similar behavior is found for the Nb 3d BE region.

The C 1s spectra of TNO in a hybrid Mg−Li battery reveal mostly pure carbon and no carbonates. A considerable LiF signal cannot be noted in either the F 1s spectrum or the Li 1s spectrum instead, the neighboring Mg 2p signal allows concluding the presence of $MgCl_2$, as confirmed by the Cl 2p spectrum. However, the Cl 2p spectrum cannot distinguish between $MgCl_2$ and phenyl chloride. After 50 cycles, a strong increase of the $MgCl_2$ peak is recognized in both Mg 2p and Cl 2p binding energy (BE) regions, indicating the growth of the chloride layer. For the hybrid Mg−Li battery, the Nb signal has decreased clearly after 50 cycles as compared to the discharged state, confirming interface growth.

Figure 7 presents the XPS quantification results of the collected data. A quite strong difference of the C content

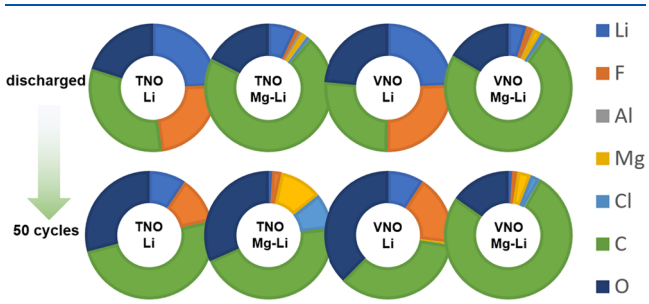

Figure 7. Elemental concentration of electrode surfaces according to XPS measurements of TNO and VNO electrodes after the first discharge and after 50 cycles in pure Li batteries and hybrid Mg−Li batteries.

between the TNO and the VNO samples cycled in hybrid Mg−Li batteries can arise from different cycling conditions: as batteries with VNO are cycled in a wider voltage window, a stronger electrolyte decomposition takes place, resulting in a larger fraction of organic decomposition products on the electrode surface.[13,45] In general, we see a domination of Li and F in lithium cells, resulting mainly from the decomposition of the $LiPF_6$ salt. However, this LiF layer is just formed in the first few cycles, and the organic decomposition products formed henceforth cover the early-stage CEI. Finally, the multilayer CEI, consisting of an inorganically dominated inner layer and the mainly organic outer layer affects the cycling stability of the materials in pure Li batteries negatively. In contrast, in hybrid cells, the formed interface contains Mg and Cl, both in proportions that still increase during cycling. It is known that chlorides can provide lower activation energies for the movement of positive charge carriers, as compared to fluorides.[46] We therefore, believe that the different characteristics of the electrode−electrolyte interlayer in the case of hybrid Mg−Li cells play a key role in providing supported diffusion for cations, leading to better cycling stability. Figure S8a provides depth profiles of XPS quantifications in the discharged state for hybrid batteries, as well as Li batteries, and Figure S8b gives depth profiles after cycling. In all cases, Nb, Ti, and V are only in traceable amounts, while carbon makes 40−70% of the interface, indicating a thick interface that exceeds the sputtered depth of up to 100 nm. However, the amount of Nb in Li- and hybrid Mg−Li batteries after cycling is comparable at the same sputtering depth, pointing at a similar thickness of the interface in both battery types. EDX elemental mappings of cycled electrodes provide further evidence for (i) the spatial distribution of Mg and Cl, superposing each other and (ii) the increasing signals of Mg and Cl after several cycles, confirming the growth of an inorganic-based CEI, see Figure S9.

It is reasonable that an optimized synthesis, producing an interconnected network of smaller particles will result in improved performance. Figure S6 shows the cycling performance of TNO, obtained from a sol−gel synthesis using the 0.4 M APC + 1.25 M LiCl electrolyte. At a high current of 1 C, the cell initially delivers 150 mAh g^{-1} and capacity retention of 90% after 100 cycles. The rate capability test (Figure S6 inset) demonstrates reduced rate dependence compared to the

https://dx.doi.org/10.1021/acs.jpcc.0c07373
J. Phys. Chem. C 2020, 124, 25239−25248

micro-sized material and an initial capacity of more than 300 mAh g^{-1} at a 0.1 C current.

4. DISCUSSION

The concept of Mg−Li hybrid batteries implies two competing mechanisms for charge storage: on the one hand, a combined insertion of both ion types into a host material and on the other hand selective charge storage, where only one type of ions (mostly Li) is involved in the insertion reaction. By increasing the particle size, one can facilitate Li insertion over Mg insertion. It is well-known that Li and Mg co-intercalation can occur into nano-sized oxide materials, as it was reported, for example, for a $Li_4Ti_5O_{12}$ spinel with nano-morphology.[47] In contrast, only Li-intercalation takes place in a micro-sized $Li_4Ti_5O_{12}$ material because the Li-diffusion in solids is generally expected to be orders of magnitude faster than Mg diffusion.[48] Within the same structural family, the electrochemical performance is highly dependent on detailed crystal features. Thus, it is not surprising that TNO outperforms VNO as it offers two additional dimensions for cation transport, reflected in a higher Li-diffusion coefficient. However, it is surprising that the Li-diffusion coefficient for each material determined in hybrid Mg−Li batteries is very similar to the value for Li batteries. It means Mg cations from the electrolyte do not influence the diffusion process significantly within the oxide electrode. However, TNO shows lower capacities in Mg−Li batteries in comparison to Li cells at the same rate for the first couple of cycles. This relates more probably to the cathode−electrolyte interface, which contains more LiF at the beginning of cycling in the case of Li cells, which is advantageous for stable cycling.[49] However, this is gradually substituted by carbonates during cycling, leading to the observed capacity loss. In contrast, the $MgCl_2$ amount in the CEI of TNO increases with cycling, thus supporting Li-diffusion and stabilizing the cycling process.

Both materials operate at low potentials, sacrificing energy density. However, according to state of the art in electrolyte development, high potential hybrid batteries are still a subject of future developments. As in the proof of concept by Yagi et al.,[3] the $LiFePO_4$ material operates at relatively high potentials, requiring the use of inert current collectors as the used electrolyte contains reactive chloride species. The need for Pt current collectors makes any prospects for industrial application unlikely.

Unfortunately, none of the proposed Mg−Li hybrid batteries that exceed a voltage of 2 V can circumvent this issue. Instead, current collectors made of molybdenum[50] or glassy carbon[51] are presented, which are as uneconomical as platinum. As long as noninert steel or copper cell parts are used, the APC-based Mg electrolyte is still the only serious candidate, and the cell chemistry has to be limited to a range within 0−2 V to ensure stability.[2] Therefore, apart from continuing the search for new electrolytes, the consistent strategy is the exploration of materials with high specific capacities to compensate for the lower voltage while still reaching high energy densities. Although rare, our observation of superior cycling performance in a dual-salt system relative to a single salt system is not unique. Recently, hybrid Na−Li electrolytes have been investigated, producing a favorable nondendritic, reversible deposition of Na only in the case of the dual-salt mixture and not for the individual components.[9] Similarly, mutual interference between Mg and Li has been reported. In an APC−LiCl electrolyte, the added Li species reduces the Mg deposition overpotential and provides Li for cathodic insertion, proving beneficial in multiple ways.[14] Herein, for the first time, we carried out a targeted analysis of the CEI formed on positive electrode materials upon cycling in hybrid Mg−Li batteries. We found this complex interface to be extremely beneficial for providing good cycling stability with superiority to the known lithium-ion battery chemistry. These insights have been assessed as highly relevant for the further application of oxide materials in hybrid Mg−Li batteries.

5. CONCLUSIONS

$TiNb_2O_7$ (TNO) and VNb_9O_{25} (VNO) were thoroughly characterized in hybrid Mg−Li batteries as well as in conventional Li-ion half cells. For both materials, better cycling stability was obtained in hybrid batteries, which is mainly attributed to similar electrolyte characteristics in terms of conductivity and desolvation energies for Li and Mg cations, similar Li-diffusion coefficients in solids, and an advantageous cathode−electrolyte interface was formed by the combination of an ether-containing electrolyte with chloride salts in Mg−Li batteries. Although the micro-sized materials deliver initial capacities of 220 mAh g^{-1} (TNO) and 150 mAh g^{-1} (VNO), sol−gel-synthesized TNO with an average particle size of 250 nm allowed to push the capacity to 300 mAh g^{-1}. Rate capability measurements, sweep rate-dependent cyclic voltammetry, and galvanostatic intermittent titration technique (GITT) results reveal superior kinetics in TNO compared to structure-related VNO. The spatial arrangement of oxygen polyhedra in the case of TNO allows better accessibility of intercalation sites and diffusion pathways as compared to VNO, which contains a relatively dense network of oxygen polyhedra. Structural peculiarities of the TNO material, together with the associated ultrafast guest cation diffusion favor its application in hybrid Mg−Li batteries in a broad temperature range suitable for stable behavior of a dual-salt electrolyte. Finally, XPS data give an insight into the composition of the interface formed on the electrodes during cycling. We identified a chloride-containing interface allowing high ionic conductivity on the electrode particle surface as the key factor for superior long-term stability of hybrid batteries, thus deepening the understanding of hybrid Mg−Li batteries, especially in terms of the interfacial properties between cathodes and electrolytes.

■ ASSOCIATED CONTENT

Supporting Information

The Supporting Information is available free of charge at https://pubs.acs.org/doi/10.1021/acs.jpcc.0c07373.

Structural parameters, comparison of different electrolyte salts, first-cycle electrochemistry, Li diffusion coefficients, current-sweep rate fits, electrochemical performance of sol−gel synthesized TNO, XPS spectra and elemental depth profiles, and EDX mapping (PDF)

■ AUTHOR INFORMATION

Corresponding Authors

Sebastian Maletti − *Leibniz Institute for Solid State and Materials Research (IFW) Dresden e.V., D-01069 Dresden, Germany;* orcid.org/0000-0001-5308-658X; Email: Sebastian.maletti@ikts-extern.fraunhofer.de

Daria Mikhailova − *Leibniz Institute for Solid State and Materials Research (IFW) Dresden e.V., D-01069 Dresden,*

https://dx.doi.org/10.1021/acs.jpcc.0c07373
J. Phys. Chem. C 2020, 124, 25239−25248

Germany; orcid.org/0000-0002-8197-1807;
Email: d.mikhailova@ifw-dresden.de

Authors

Abraham Herzog-Arbeitman − *Leibniz Institute for Solid State and Materials Research (IFW) Dresden e.V., D-01069 Dresden, Germany; Department of Chemistry, University of Chicago, Chicago, Illinois 60637, United States;* orcid.org/0000-0001-6238-7413

Steffen Oswald − *Leibniz Institute for Solid State and Materials Research (IFW) Dresden e.V., D-01069 Dresden, Germany*

Anatoliy Senyshyn − *Forschungs-Neutronenquelle Heinz Maier-Leibnitz FRM-II, Technische Universität München, D-85747 Garching bei München, Germany*

Lars Giebeler − *Leibniz Institute for Solid State and Materials Research (IFW) Dresden e.V., D-01069 Dresden, Germany;* orcid.org/0000-0002-6703-8447

Complete contact information is available at: https://pubs.acs.org/10.1021/acs.jpcc.0c07373

Notes

The authors declare no competing financial interest.

■ ACKNOWLEDGMENTS

We would like to acknowledge Haneen Albukai and Ronny Buckan (both IFW Dresden) for assistance with electrochemical experiments. This project has benefitted from the European Union and the Free State of Saxony under the TTKin project (SAB Grant no. 100225299).

■ REFERENCES

(1) Aurbach, D.; Lu, Z.; Schechter, A.; Gofer, Y.; Gizbar, H.; Turgeman, R.; Cohen, Y.; Moshkovich, M.; Levi, E. Prototype systems for rechargeable magnesium batteries. *Nature* **2000**, *407*, 724−727.

(2) Muldoon, J.; Bucur, C. B.; Gregory, T. Fervent Hype behind Magnesium Batteries: An Open Call to Synthetic Chemists-Electrolytes and Cathodes Needed. *Angew. Chem., Int. Ed.* **2017**, *56*, 12064−12084.

(3) Yagi, S.; Ichitsubo, T.; Shirai, Y.; Yanai, S.; Doi, T.; Murase, K.; Matsubara, E. A concept of dual-salt polyvalent-metal storage battery. *J. Mater. Chem. A* **2014**, *2*, 1144−1149.

(4) Cheng, Y.; Chang, H. J.; Dong, H.; Choi, D.; Sprenkle, V. L.; Liu, J.; Yao, Y.; Li, G. Rechargeable Mg−Li hybrid batteries: status and challenges. *J. Mater. Res.* **2016**, *31*, 3125−3141.

(5) Cheng, Y.; Shao, Y.; Zhang, J.-G.; Sprenkle, V. L.; Liu, J.; Li, G. High performance batteries based on hybrid magnesium and lithium chemistry. *Chem. Commun.* **2014**, *50*, 9644−9646.

(6) Cho, J.-H.; Aykol, M.; Kim, S.; Ha, J.-H.; Wolverton, C.; Chung, K. Y.; Kim, K.-B.; Cho, B.-W. Controlling the intercalation chemistry to design high-performance dual-salt hybrid rechargeable batteries. *J. Am. Chem. Soc.* **2014**, *136*, 16116−16119.

(7) Ichitsubo, T.; Okamoto, S.; Kawaguchi, T.; Kumagai, Y.; Oba, F.; Yagi, S.; Goto, N.; Doi, T.; Matsubara, E. Toward "rocking-chair type" Mg−Li dual-salt batteries. *J. Mater. Chem. A* **2015**, *3*, 10188−10194.

(8) Fu, Q.; Azmi, R.; Sarapulova, A.; Mikhailova, D.; Dsoke, S.; Missiul, A.; Trouillet, V.; Knapp, M.; Bramnik, N.; Ehrenberg, H. Electrochemical and structural investigations of different polymorphs of TiO_2 in magnesium and hybrid lithium/magnesium batteries. *Electrochim. Acta* **2018**, *277*, 20−29.

(9) Zhang, Q.; Lu, Y.; Miao, L.; Zhao, Q.; Xia, K.; Liang, J.; Chou, S.-L.; Chen, J. An Alternative to Lithium Metal Anodes: Non-dendritic and Highly Reversible Sodium Metal Anodes for Li-Na Hybrid Batteries. *Angew. Chem., Int. Ed.* **2018**, *57*, 14796−14800.

(10) Cen, Y.; Liu, Y.; Zhou, Y.; Tang, L.; Jiang, P.; Hu, J.; Xiang, Q.; Hu, B.; Xu, C.; Yu, D.; et al. Spinel $Li_4Mn_5O_{12}$ as 2.0 V Insertion Materials for Mg-Based Hybrid Ion Batteries. *ChemElectroChem* **2020**, *7*, 1115−1124.

(11) Rajput, N. N.; Seguin, T. J.; Wood, B. M.; Qu, X.; Persson, K. A. Elucidating Solvation Structures for Rational Design of Multivalent Electrolytes-A Review. *Top. Curr. Chem.* **2018**, *376*, 19.

(12) Mizrahi, O.; Amir, N.; Pollak, E.; Chusid, O.; Marks, V.; Gottlieb, H.; Larush, L.; Zinigrad, E.; Aurbach, D. Electrolyte Solutions with a Wide Electrochemical Window for Rechargeable Magnesium Batteries. *J. Electrochem. Soc.* **2008**, *155*, A103−A109.

(13) Lipson, A. L.; Han, S.-D.; Pan, B.; See, K. A.; Gewirth, A. A.; Liao, C.; Vaughey, J. T.; Ingram, B. J. Practical Stability Limits of Magnesium Electrolytes. *J. Electrochem. Soc.* **2016**, *163*, A2253−A2257.

(14) Yoo, H. D.; Shterenberg, I.; Gofer, Y.; Doe, R. E.; Fischer, C. C.; Ceder, G.; Aurbach, D. A Magnesium-Activated Carbon Hybrid Capacitor. *J. Electrochem. Soc.* **2014**, *161*, A410−A415.

(15) Duffort, V.; Sun, X.; Nazar, L. F. Screening for positive electrodes for magnesium batteries: a protocol for studies at elevated temperatures. *Chem. Commun.* **2016**, *52*, 12458−12461.

(16) Miao, X.; Chen, Z.; Wang, N.; Nuli, Y.; Wang, J.; Yang, J.; Hirano, S.-i. Electrospun V_2MoO_8 as a cathode material for rechargeable batteries with Mg metal anode. *Nano Energy* **2017**, *34*, 26−35.

(17) Rashad, M.; Zhang, H.; Li, X.; Zhang, H. Fast kinetics of Mg^{2+}/Li^+ hybrid ions in a polyanion $Li_3V_2(PO_4)_3$ cathode in a wide temperature range. *J. Mater. Chem. A* **2019**, *7*, 9968−9976.

(18) Come, J.; Augustyn, V.; Kim, J. W.; Rozier, P.; Taberna, P.-L.; Gogotsi, P.; Long, J. W.; Dunn, B.; Simon, P. Electrochemical Kinetics of Nanostructured Nb_2O_5 Electrodes. *J. Electrochem. Soc.* **2014**, *161*, A718−A725.

(19) Hu, L.; Luo, L.; Tang, L.; Lin, C.; Li, R.; Chen, Y. $Ti_2Nb_{2x}O_{4+5x}$ anode materials for lithium-ion batteries: a comprehensive review. *J. Mater. Chem. A* **2018**, *6*, 9799−9815.

(20) Han, J.-T.; Goodenough, J. B. 3-V Full Cell Performance of Anode Framework $TiNb_2O_7$/Spinel $LiNi_{0.5}Mn_{1.5}O_4$. *Chem. Mater.* **2011**, *23*, 3404−3407.

(21) Qian, S.; Yu, H.; Yan, L.; Zhu, H.; Cheng, X.; Xie, Y.; Long, N.; Shui, M.; Shu, J. High-Rate Long-Life Pored Nanoribbon VNb_9O_{25} Built by Interconnected Ultrafine Nanoparticles as Anode for Lithium-Ion Batteries. *ACS Appl. Mater. Interfaces* **2017**, *9*, 30608−30616.

(22) Jiang, C.; Liu, T.; Long, N.; Cheng, X.; Peng, N.; Zhang, J.; Zheng, R.; Yu, H.; Shu, J. VNb_9O_{25} nanowires with superior electrochemical property towards lithium ion batteries. *Ceram. Int.* **2019**, *45*, 18111−18114.

(23) Patoux, S.; Masquelier, C. Chemical and Electrochemical Insertion of Lithium into Two Allotropic Varieties of $NbPO_5$. *Chem. Mater.* **2002**, *14*, 2334−2341.

(24) Hoelzel, M.; Senyshyn, A.; Juenke, N.; Boysen, H.; Schmahl, W.; Fuess, H. High-resolution neutron powder diffractometer SPODI at research reactor FRM II. *Nucl. Instrum. Methods Phys. Res., Sect. A* **2012**, *667*, 32−37.

(25) Roisnel, T.; Rodríquez-Carvajal, J. WinPLOTR: A Windows Tool for Powder Diffraction Pattern Analysis. *Mater. Sci. Forum* **2001**, *378*−*381*, 118−123.

(26) Moulder, J. F.; Stickle, W. F.; Sobol, P. E.; Kenneth, D. B. *Handbook of X-ray Photoelectron Spectroscopy*; Perkin-Elmer Corporation: Eden Prairie, 1992.

(27) Wadsley, A. D. Mixed oxides of titanium and niobium. I. *Acta Crystallogr.* **1961**, *14*, 660−664.

(28) Polte, A.; Langbein, H. Zur Bildung und Umwandlung von Oxidphasen im quasibinren System V_2O_5-Nb_2O_5. *Z. Anorg. Allg. Chem.* **1994**, *620*, 1947−1952.

(29) Deng, Q.; Fu, Y.; Zhu, C.; Yu, Y. Niobium-Based Oxides Toward Advanced Electrochemical Energy Storage: Recent Advances and Challenges. *Small* **2019**, *15*, No. 1804884.

(30) van Orman, J. A.; Crispin, K. L. Diffusion in Oxides. *Rev. Mineral. Geochem.* **2010**, *72*, 757−825.
(31) Bard, A. J.; Faulkner, L. R. *Electrochemical Methods: Fundamentals and Applications*, 2nd ed.; John Wiley & Sons, Inc.: New York, 2001.
(32) Lin, C.; Hu, L.; Cheng, C.; Sun, K.; Guo, X.; Shao, Q.; Li, J.; Wang, N.; Guo, Z. Nano-$TiNb_2O_7$/carbon nanotubes composite anode for enhanced lithium-ion storage. *Electrochim. Acta* **2018**, *260*, 65−72.
(33) Liu, T.-C.; et al. Behavior of Molybdenum Nitrides as Materials for Electrochemical Capacitors. *J. Electrochem. Soc.* **1998**, *145*, 1882−1888.
(34) Conway, B. E.; Pell, W. G. Double-layer and pseudocapacitance types of electrochemical capacitors and their applications to the development of hybrid devices. *J. Solid State Electrochem.* **2003**, *7*, 637−644.
(35) Lou, S.; Cheng, X.; Zhao, Y.; Lushington, A.; Gao, J.; Li, Q.; Zuo, P.; Wang, B.; Gao, Y.; Ma, Y.; et al. Superior performance of ordered macroporous $TiNb_2O_7$ anodes for lithium ion batteries: Understanding from the structural and pseudocapacitive insights on achieving high rate capability. *Nano Energy* **2017**, *34*, 15−25.
(36) Babu, B.; Shaijumon, M. M. Studies on kinetics and diffusion characteristics of lithium ions in $TiNb_2O_7$. *Electrochim. Acta* **2020**, *345*, No. 136208.
(37) Augustyn, V.; Come, J.; Lowe, M. A.; Kim, J. W.; Taberna, P.-L.; Tolbert, S. H.; Abruña, H. D.; Simon, P.; Dunn, B. High-rate electrochemical energy storage through Li^+ intercalation pseudocapacitance. *Nat. Mater.* **2013**, *12*, 518−522.
(38) Canepa, P.; Gautam, G. S.; Malik, R.; Jayaraman, S.; Rong, Z.; Zavadil, K. R.; Persson, K.; Ceder, G. Understanding the Initial Stages of Reversible Mg Deposition and Stripping in Inorganic Nonaqueous Electrolytes. *Chem. Mater.* **2015**, *27*, 3317−3325.
(39) Xu, K. Charge-Transfer" Process at Graphite/Electrolyte Interface and the Solvation Sheath Structure of Li^+ in Nonaqueous Electrolytes. *J. Electrochem. Soc.* **2007**, *154*, A162−A167.
(40) Iermakova, D. I.; Dugas, R.; Palacín, M. R.; Ponrouch, A. On the Comparative Stability of Li and Na Metal Anode Interfaces in Conventional Alkyl Carbonate Electrolytes. *J. Electrochem. Soc.* **2015**, *162*, A7060−A7066.
(41) Nie, M.; Lucht, B. L. Role of Lithium Salt on Solid Electrolyte Interface (SEI) Formation and Structure in Lithium Ion Batteries. *J. Electrochem. Soc.* **2014**, *161*, A1001−A1006.
(42) Karakalos, S.; Siokou, A.; Ladas, S. The interfacial properties of $MgCl_2$ films grown on a flat SiO_2/Si substrate. An XPS and ISS study. *Appl. Surf. Sci* **2009**, *255*, 8941−8946.
(43) Khattak, G. D.; Salim, M. A.; Al-Harthi, A. S.; Thompson, D. J.; Wenger, L. E. Structure of molybdenum-phosphate glasses by X-ray photoelectron spectroscopy (XPS). *J. Non-cryst. Solids* **1997**, *212*, 180−191.
(44) Eshkenazi, V.; Peled, E.; Burstein, L.; Golodnitsky, D. XPS analysis of the SEI formed on carbonaceous materials. *Solid State Ionics* **2004**, *170*, 83−91.
(45) Lu, Z.; Schechter, A.; Moshkovich, M.; Aurbach, D. On the electrochemical behavior of magnesium electrodes in polar aprotic electrolyte solutions. *J. Electroanal. Chem.* **1999**, *466*, 203−217.
(46) Kittel, C. *Einführung in die Festkörperphysik*, 15., unveränderte Aufl.; Oldenbourg Verlag: München, 2013.
(47) Yao, H.-R.; You, Y.; Yin, Y.-X.; Wan, L.-J.; Guo, Y.-G. Rechargeable dual-metal-ion batteries for advanced energy storage. *Phys. Chem. Chem. Phys.* **2016**, *18*, 9326−9333.
(48) Mehrer, H. *Diffusion in Solids: Fundamentals, Methods, Materials, Diffusion-controlled Processes*; Springer Series in Solid-State Sciences; Springer: Dordrecht, 2007; Vol. *33*.
(49) Choudhury, S.; Archer, L. A. Lithium Fluoride Additives for Stable Cycling of Lithium Batteries at High Current Densities. *Adv. Electron. Mater.* **2016**, *2*, No. 1500246.
(50) Cheng, Y.; Choi, D.; Han, K. S.; Mueller, K. T.; Zhang, J.-G.; Sprenkle, V. L.; Liu, J.; Li, G. Toward the design of high voltage magnesium−lithium hybrid batteries using dual-salt electrolytes. *Chem. Commun.* **2016**, *52*, 5379−5382.
(51) Yan, J.; Wang, J.; Liu, H.; Bakenov, Z.; Gosselink, D.; Chen, P. Rechargeable hybrid aqueous batteries. *J. Power Sources* **2012**, *216*, 222−226.

https://dx.doi.org/10.1021/acs.jpcc.0c07373
J. Phys. Chem. C 2020, 124, 25239−25248